Check for updates

JGR Atmospheres

RESEARCH ARTICLE
10.1029/2020JD033268

Mesospheric Mountain Wave Activity in the Lee of the Southern Andes

P.-D. Pautet[1], M. J. Taylor[1], D. C. Fritts[2], D. Janches[3], N. Kaifler[4], A. Dörnbrack[4], and J. L. Hormaechea[5]

[1]Center for Atmospheric and Space Sciences/Physics Department, State University, Logan, UT, USA, [2]GATS, Boulder, CO, USA, [3]NASA GSFC, Washington, DC, USA, [4]Deutsches Zentrum für Luft- und Raumfahrt, Oberpfaffenhaufen, Germany, [5]Universidad Nacional de Tierra del Fuego, Rio Grande, Argentina

Key Points:

- Numerous mesospheric mountain waves observed in the lee of the Southern Andes, a major gravity waves hotspot, under wintertime conditions
- Mountain wave occurrence is highly correlated with the eastward phase of the semi-diurnal tide in the upper mesosphere
- Mountain wave momentum fluxes can reach very large values, revealing their major impact on the upper atmosphere

Correspondence to:
P.-D. Pautet,
dominiquepautet@gmail.com

Citation:
Pautet, P.-D., Taylor, M. J., Fritts, D. C., Janches, D., Kaifler, N., Dörnbrack, A., & Hormaechea, J. L. (2021). Mesospheric mountain wave activity in the lee of the Southern Andes. *Journal of Geophysical Research: Atmospheres*, *126*, e2020JD033268. https://doi.org/10.1029/2020JD033268

Received 11 JUN 2020
Accepted 23 OCT 2020

© 2021. American Geophysical Union. All Rights Reserved.

Abstract Gravity waves (GWs) generated by orographic forcing, also known as mountain waves (MWs) have been studied for decades. First measured in the troposphere, then in the stratosphere, they were only imaged at mesospheric altitude in 2008. Their characteristics have been investigated during several recent observation campaigns, but many questions remain concerning their impacts on the upper atmosphere, and the effects of the background environment on their deep propagation. An Advanced Mesospheric Temperature Mapper (AMTM) and the Southern Argentina Agile MEteor Radar (SAAMER) have been operated simultaneously during the Austral winter 2018 from Rio Grande, Argentina (53.8°S). This site is located near the tip of South America, in the lee of the Andes Mountains, a region considered the largest MW hotspot on Earth (e.g., Eckermann & Preusse, 1999; Hendricks et al., 2014; Jiang et al., 2003, 2005, 2002; Wright et al., 2016). New AMTM image data obtained during a 6-month period show almost 100 occurrences of MW signatures penetrating into the upper mesosphere. They are visible ∼30% of time during the period corresponding to the middle of the winter season (mid-May to mid-July). Their intermittency is highly correlated with the zonal wind controlled by the semi-diurnal tide, revealing the direct effect of the atmospheric background on MW penetration into the mesosphere lower thermosphere (MLT, altitude 80–100 km). Measurements of their momentum fluxes (MFs) were determined to reach very large values (average for 36 events ∼250 m^2/s^2), providing strong evidence of the importance and impacts of small-scale gravity waves at mesospheric altitudes.

1. Introduction

Gravity waves (GWs) are major contributors to middle and upper atmosphere dynamics because they account for large momentum and energy transports from sources at lower altitudes, and systematic and variable momentum and energy deposition where they dissipate. Mean seasonal GW momentum deposition closes the polar mesospheric jets, inducing a pole-to-pole residual circulation, and driving large-scale constituent transport and mean temperatures far from radiative equilibrium (Fritts & Alexander, 2003). GW energy dissipation accompanies breaking and leads to a range of instabilities, turbulence, and local heating and mixing. Their importance has been increasingly recognized over the past six decades, but many GW dynamics and effects have yet to be understood and quantified.

GWs have many sources accompanying weather events in the troposphere and lower stratosphere. Of these, air flow over orography that generates mountain waves (MWs) yields the most significant local and statistical responses from the tropopause to the upper stratosphere based on global in situ and remote-sensing measurements (Eckermann & Preusse, 1999; Fritts & Nastrom, 1992; Hertzog et al., 2012; Jiang et al., 2002).

Tropospheric MWs have been discovered in the 1930s by glider pilots flying over Central Europe (Küttner, 1939a, 1939b). Numerous theoretical studies and airborne observations followed, aimed at understanding the vertical propagation of these waves and the hazards they create on air transport (e.g., Eliassen & Palm, 1960; Grubišić et al., 2008; Scorer, 1949; Smith, 1980, 2019 and references herein). It was only in the 1990s that MWs were measured in the stratosphere using airborne backscatter lidar, radiosonde, balloon, or satellite data (e.g., Alexander & Teitelbaum, 2011; Dörnbrack et al., 2002, 1999; Eckermann & Preusse, 1999; Plougonven et al., 2008; Wu et al., 2006). First mesospheric observations were reported over the El Leoncito Observatory, Argentina, in 2008 (Smith et al., 2009) using airglow image data. Recent satellite measurements

over the Southern Andes coupled with raytracing technique, have shown that MWs can even affect the thermosphere (upto ~275 km) through secondary, tertiary or higher-order GW originating from MW breaking (Vadas et al., 2019).

Since, individual instruments have performed more observations, contributing useful, but less comprehensive measurements. Clusters of instruments or dedicated campaigns have enabled much greater and more extensive quantification of MW events and their consequences. Novel imaging, radar and lidar technologies, as well as parallel modeling, are allowing further advances addressing key remaining needs: further investigations can reveal more about the characteristics and variability of major sources and the filtering effects of the background atmosphere.

The characteristics of these MWs at lower altitudes are directly related to the three-dimensional structure of the terrain and the strength of the airflow. However, their responses at higher altitudes depend on the horizontal wind and temperature fields through which they propagate, and with which they often interact strongly (Bramberger et al., 2017; Kruse et al., 2016). Under winter conditions, zonal winds are typically eastward throughout the stratosphere and into the mesosphere from middle to high latitudes, but with magnitudes that vary due to weather systems at lower altitudes and to global planetary waves at higher altitudes.

When zonal winds are eastward and increase strongly in the stratosphere, recent coordinated measurements during the NFS DEEPWAVE campaign (Fritts et al., 2016) have shown that MWs can easily amplify into the mesosphere and attain breaking amplitudes in decreasing winds above (Eckermann et al., 2016; Fritts et al., 2019, 2018; Pautet et al., 2016; Taylor et al., 2019). Weaker or decreasing zonal winds in the stratosphere constrain their amplitudes, but the surviving MWs can nevertheless enable large responses at higher altitudes due to amplitude growth where zonal winds are increasing (Bramberger et al., 2017; Kruse et al., 2016). This is possible because MWs (and generally GWs) undergo breaking at a horizontal perturbation amplitude of $|u_h'| \sim |c\text{-}U_h|$, for phase speed c and horizontal mean wind U_h, with a critical level being a special case causing full GW dissipation. Where $|c\text{-}U_h|$ remains >0, breaking does not eliminate the GW, but likely generate secondary GWs. The surviving GW grows again with increasing $|c\text{-}U_h|$ and altitude. As a consequence, MW deep penetration into the middle and upper atmosphere can only happen during the winter season, when the zonal wind stays eastward up to the mesosphere lower thermosphere (MLT) (Schoeberl, 1985; Scorer, 1949; Smith et al., 2009).

In 2009, Smith et al. showed, using all-sky airglow image data taken in the lee side of the Andes (31.8°S), that MWs can occasionally reach mesospheric altitudes. They observed stationary waves, parallel to the mountain range, several days in a row during the month of July 2008. More recently, several projects including the Deep Propagating Gravity Wave Experiment (DEEPWAVE), and measurements obtained from the Andes Lidar Observatory (ALO, 30.2°S) in Chile, provided more insight on MW propagation into the MLT (Fritts et al., 2016; Hecht et al., 2018). Surprising results including the scale and extent of these MWs (Bossert et al., 2015), or their effects on the upper atmosphere (Eckermann et al., 2016; Fritts et al., 2018; Pautet et al., 2016; Taylor et al., 2019) have been recently published.

One of the most interesting results is the intermittent nature of MW occurrence in the mesosphere. Even when the tropospheric forcing persisted several days, MWs were not observed continuously in the MLT during the same period. They appeared and disappeared, as if a gate was opening and closing, blocking their propagation at a lower level or allowing them to penetrate higher up. This result yields the following question: what are the most favorable background atmosphere conditions for MW deep propagation? To answer this question, it is necessary to obtain simultaneous measurements from collocated instruments operating close to a MW hotspot.

There are many specific regions on Earth where a variety of MW responses can be observed, but the largest hotspot is located over the southern part of South America during austral winter. Multiple studies have shown that strong tropospheric winds blowing over the Andes generate large orographic responses in the MLT under suitable propagation conditions (e.g., Alexander & Teitelbaum, 2011; Eckermann & Preusse, 1999; Jiang et al., 2002; Wright et al., 2016). Similar Southern Hemisphere (SH) responses also occur over New Zealand, and are likely over smaller SH islands at higher latitudes, and the coast of

Antarctica, given their signatures in the stratosphere (Hendricks et al., 2014), but some of them have yet to be observed in the MLT.

A cluster of novel, high quality instrumentation exists in the lee of the Southern Andes. In Rio Grande, Argentina (53.8°S), a meteor radar (Gats Inc., USA), a Rayleigh lidar (Deutsches Zentrum für Luft- und Raumfahrt, DLR, Germany), an AMTM (Utah state University, USU), and a multi-wavelength all-sky airglow imager (Boston University, BU, USA) have operated jointly since November 2017. During the Austral winter 2018 (mid-March to mid-September) 97 MW signatures were recorded in AMTM image data, allowing for the investigation of the atmospheric conditions conducive to MW deep propagation.

This paper presents these new MW observations, and shows the strong correlation between their occurrence in the mesosphere and the eastward zonal wind, which was found to be mostly controlled by the semi diurnal tide. Section 2 will give an overview of the observation site and the instruments involved in this study. Section 3 will describe the observations, which will be discussed in Section 4. Finally, conclusions will be given in Section 5.

2. Instrumentation

2.1. Estación Astronómica Rio Grande (EARG)

The Rio Grande Observatory (53.8°S, 67.7°W) or Estación Astronómica Rio Grande (EARG) is located in southern Argentina, in the region known as Tierra del Fuego. This site is in close proximity to a massive knife edge-like mountain chain near-continuously exposed to strong and persistent circumpolar winds, making it part of the most active GW hotspot on Earth (with multiple peaks >1,600 m located ∼160 km to the West-South-West, and a more moderate region with peaks <1,000 m, ∼300 km to the West). The latitude also allows for year-round measurements (no permanent twilight during summer) using autonomous instrument operations.

2.2. Advanced Mesospheric Temperature Mapper

One of the instruments operating at this site, the USU Advanced Mesospheric Temperature Mapper measures the nighttime atmospheric temperature over a ∼200 × 160 km region centered at the zenith, using the OH (3,1) band emission (Pautet et al., 2014). This bright emission originates from a ∼7 to 8 km-thick layer located at ∼87 km altitude, and is widely used as a tracer of the dynamical processes in the MLT. The AMTM was designed and built at Utah State University. It uses a 320 × 256-pixel infrared sensor and a computer-controlled filter wheel to sequentially measure the brightness of the $P_1(2)$ and $P_1(4)$ lines of the OH (3,1) band, as well as the atmospheric background. Combining these three emissions, it is possible to process the OH (3,1) rotational temperature for each pixel of an image and "map" the mesospheric temperature over a large region. Its high spatial (∼0.625 km/pix) and temporal (1 temperature map every ∼35 s) resolutions, and high precision (∼1 K) allow to measure small and medium-scale GWs characteristics, study GW dissipation and breaking/instabilities, and assess the momentum flux carried by GW events (e.g., Bossert et al., 2015; Fritts et al., 2014; Pautet et al., 2018, 2016; Taylor et al., 2019; Zhao et al., 2019). The AMTM instrument was installed in November 2017 and has operated almost continuously since then.

2.3. SAAMER Momentum Flux Radar

The Southern Argentina Agile MEteor Radar (SAAMER) was designed specifically to enable very high-resolution definition of the large-scale wind field and potential sensitivity to GW momentum fluxes employing a generalization of the dual-beam technique (Fritts, Janches, Iimura et al., 2010). Its frequency and bandwidth are 32.55 and 0.3 MHz, respectively. The transmitter antenna is composed of eight 3-element crossed Yagis arranged in a 27.6 m diameter circle. Its transmit/receive (T/R) switch allows both tropospheric and mesospheric measurements, and the use of the transmitter antennas as a sixth receiver. It is able to measure neutral vertical velocities in the troposphere and MLT. SAAMER has operated at Rio Grande since May

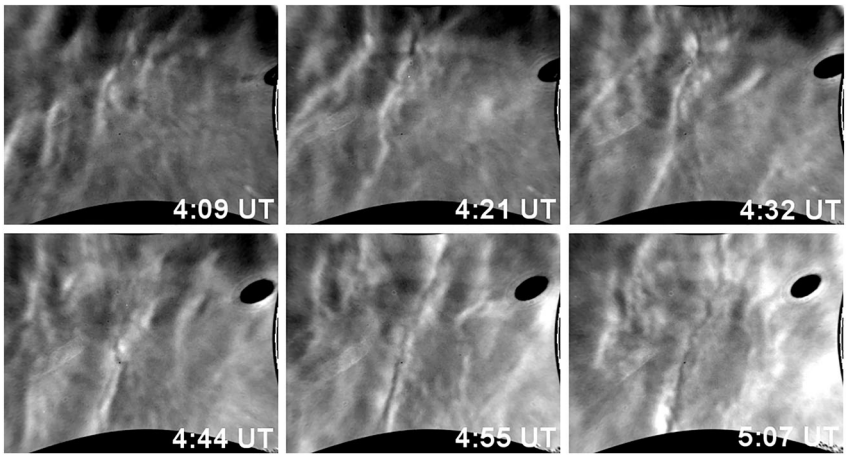

Figure 1. Series of OH (3,1) temperature maps (at ~12 min intervals) showing the quasi stationary signature of a mesospheric mountain wave event which occurred on the night of June 02 and 03, 2018. The black region at the bottom of the images is due to the projection technique, and the black spot moving westward is the full moon.

2008. It provides horizontal wind data between ~80 and 100 km (de Wit et al., 2016, 2017; Fritts, Janches, & Hocking 2010; Wright et al., 2016).

3. Observations—Results

3.1. Mountain Wave Observations

The OH (3,1) rotational temperature and band intensity were mapped every night during the Austral winter 2018 using the AMTM. In airglow image data, MWs appear as nearly stationary waves that can last several hours, as shown in Figure 1. For easier MW identification, keogram images were automatically generated to summarize each night of observation. These were created by taking the central rows and columns of a series of pictures, and collocating them to produce north–south (NS) and west–east (WE) keogram images, respectively (Taylor et al., 2009). MWs appear as nearly horizontal bands in the WE keogram (because of their near-zero observed zonal phase speed). For example, Figure 2 shows WE keograms in temperature (Figure 2a) and brightness (Figure 2b) for the night of May 21 and 22, 2018. MW structures are visible until 22:30 UT, and between ~3:00 and ~9:00 UT. Red contours help localize them in the brightness image. After initial identification in the keograms, each MW occurrence was confirmed by looking at the image data. To be tagged as a MW event, a GW had to last at least 1 h (to avoid confusion with possible long lasting instability features, or so-called ripples), with an average horizontal phase speed < 10 m/s for its whole duration. MWs are not perfectly stationary because of their nonlinear response to horizontal wind variations, so a 10 m/s uncertainty allows for their detection but is still below the horizontal phase speed of most nonorographic GWs.

During the period mid-March to mid-September 2018, which encompasses the Austral winter season, a total of 97 MW events were detected during 78 nights, the earliest being March 30–31, and the latest September 05 and 06. Such a large number was unexpected but confirms previous, more limited AMTM ground-based observations made from Lauder, New Zealand, as part of the DEEPWAVE campaign. During that project, which comprised 53 nights of observation (May 30 and 31 to July 21 and 22, 2014), 28 of the 44 clear or partially clear nights showed signs of MWs (64%) (Taylor et al., 2019), providing a first evidence of their potential significant importance at mesospheric altitudes.

To have a better idea of the occurrence frequency of MWs over Rio Grande, their duration was compared to the total hours of clear sky during the nighttime for the considered 6-month period. Figure 3 shows the evolution of the MW detection vs the hours of clear sky over the observatory. Viewing conditions were good for 1,314 h (57.5% of the 2,285 h of dark sky observations during these 6 months), with MWs visible in the AMTM data during 339 h, corresponding to 25.8%. This value was highly variable, with most MWs

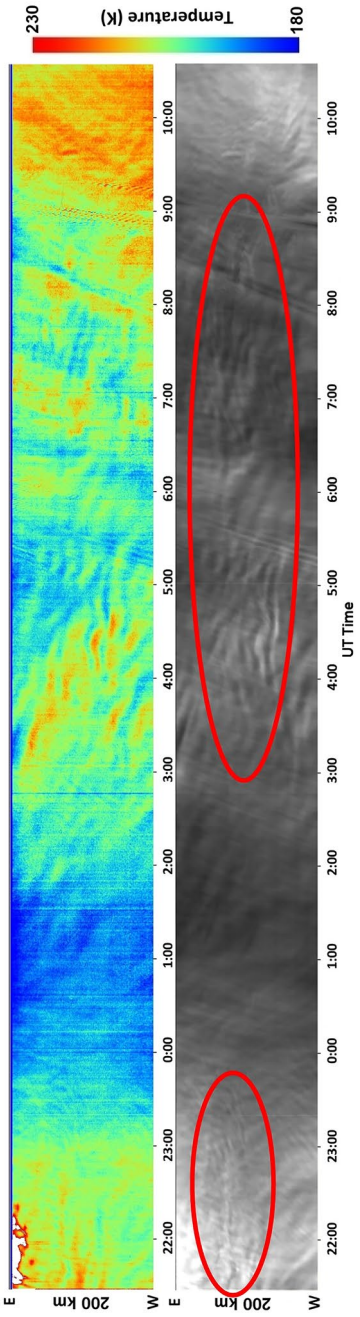

Figure 2. Keogram images summarizing the observations for the night of May 21 and 22, 2018. Top: OH rotation temperature, Bottom: OH brightness. Mountain waves appear as horizontal bands between 22:30 UT and between 3:00 and 9:00 UT . They are emphasized with red loops on the brightness keogram (bottom).

occurring between mid-May and mid-July (~35%), and more sporadic events detected before and after this period.

MWs observed over Rio Grande exhibit various structures and/or behaviors. Figure 4 shows six examples of the MW patterns recorded during the winter 2018: Small-scale waves (λ_h < ~20 km) localized within a wider band (Figure 4a), middle size waves (~20 < λ_h < ~50 km) covering the whole field-of-view (Figure 4b), so-called "sawtooth pattern" (Figure 4c) exhibiting narrow cold regions characteristic of overturning waves, and similar to structures previously observed over New Zealand (Taylor et al., 2019), coincident observations of two different types of structures (Figure 4d), MW breaking over a large region (4e), and MWs associated with streamwise-aligned instabilities (Figure 4f) (Fritts et al., 2019). Each of these types were observed several times during the 2018 winter season and seemed to correspond to different MW generation and propagation conditions.

The MW parameters (horizontal wavelength λ_h, direction of propagation φ, and temperature perturbation T') were measured using well-developed Fast Fourier Transform (FFT) technique. Results are shown in Figure 5. Because of their nature, MW observed phase speeds are close to zero (e.g., Smith, 2019; Smith et al., 2009), thus not included in the figure. Furthermore, the FFT analysis gives a 180° ambiguity in the direction of propagation, but the eastward tropospheric wind forcing generates westward-propagating MWs and continuous eastward winds at higher altitudes are required to enable MWs to propagate into the mesosphere, thus propagation directions must be between 180° and 360°.

The MW horizontal wavelengths are of the same order (a mean of 25.6 km) as previous airglow nonorographic GW measurements from mid-latitude sites, which ranged between 20 and 30 km for most events (e.g., Hecht et al., 2001 at 40°N; Stockwell & Lowe, 2001 at 42°N; Ejiri et al., 2003 at 35°N and 44°N). The horizontal wavelengths observed in previous MW studies, all of which investigated individual events, varied from 25 km (Bossert et al., 2015), to 36 km (Smith et al., 2009), 40 km (Pautet et al., 2016), 40–71 km (Taylor et al., 2019), and up to ~240 km (Bossert et al., 2015, 2017; Fritts et al., 2018). The larger scales were only observable because the imagers were on a moving platform. The AMTM field-of-view (200 × 160 km) limits the unambiguous detection of MWs to λ_h < 100 km. Larger MWs have a more limited impact on the upper atmosphere, though, with much smaller momentum flux (MF) values (Bossert et al., 2015; Fritts et al., 2018).

MW directionality is as expected for this site, with an average direction of propagation equal to 268°(σ = 21°), consistent with an eastward tropospheric wind forcing over the Southern Andes and sustained eastward wind above. There is some variability, though, with values ranging between ~227° and ~318°, which can be explained by irregularities in the direction and amplitude of the forcing, the three-dimensional character of the Southern Andes, and the variability of the atmospheric background between the troposphere and the mesosphere.

The average<T'> is 5.0 K (σ = 3.1 K), with 94% of the amplitudes < 10 K, and a maximum at ~17 K. These are similar to previously published MW T' measurements (e.g., Bossert et al., 2015, 4 < T' < 8 K, Pautet et al., 2016, T' ~ 10 K), but much smaller than the spectacular event described by Taylor et al. (2019), which reached an amplitude of ~37 K.

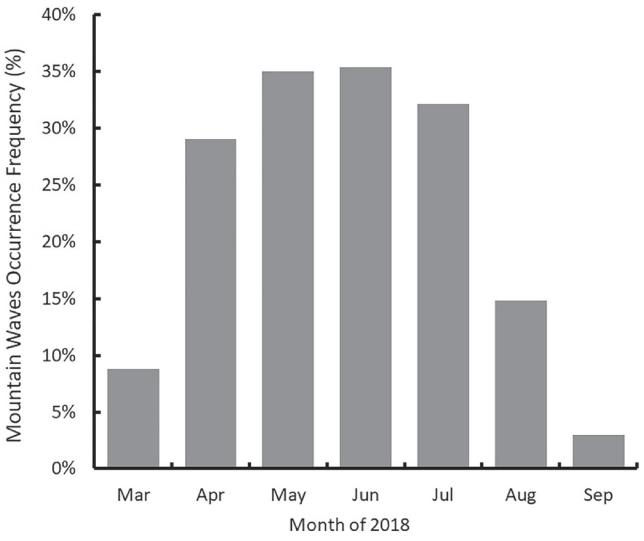

Figure 3. Mountain wave occurrence vs hours of clear sky between March 15, 2018 and September 15, 2018.

3.2. Momentum Flux Calculations

As MWs propagate upward, they transport momentum that resides in the background atmosphere via a pseudo-momentum flux (MF) (Fritts & Alexander, 2003). The MF per unit mass$<u_h'w'>$ for a given wave can be calculated knowing its parameters, as well as the background conditions, using the following equation (Fritts et al., 2014)

$$\langle u_h'w' \rangle = \frac{g^2 \omega_i}{2N^3} \sqrt{1 - \frac{\omega_i^2}{N^2}} \left(\frac{\langle T' \rangle}{T_0} \right)^2 \frac{1}{C^2}. \quad (1)$$

here g is the acceleration of gravity (9.54 ms^{-2} at the OH layer), N is the buoyancy frequency, ω_i is the intrinsic frequency, $<T'>$ is the measured temperature perturbation amplitude, T_0 the mean temperature at the altitude of the OH (3,1) emission, and C is a factor to compensate for the phase averaging over the finite thickness of the OH layer. It is defined by

$$C = \frac{\langle T' \rangle}{T'(z_0)} = \exp\left(-3.56 \frac{z_{FWHM}^2}{\lambda_z^2} \right) \quad (2)$$

where Z_{FWHM} is the full-width half-maximum OH layer thickness (~7 km) and λ_z is the MW vertical wavelength. The triangular parentheses in Equation 1 represent means over both the airglow layer and a complete wave oscillation.

At Rio Grande, the AMTM instrument provided direct measurements of the MW horizontal parameters (wavelength λ_h, direction of propagation φ, temperature perturbation $<T'>$). SAAMER measured the background meridional and zonal wind speed amplitudes u and v, respectively. The buoyancy frequency N was taken equal to 0.02 ± 0.002 s^{-1} for all the calculations, corresponding to a buoyancy period of ~5 min, typical at this altitude. The vertical wavelength λ_z was then calculated using a simplified version of the dispersion relation, neglecting the wind shear and the wind curvature (smoothly and gradually varying background wind speed, Nappo, 2002)

$$m^2 = \frac{N^2}{(c - U_h)^2} - \frac{1}{4H^2} - k^2. \quad (3)$$

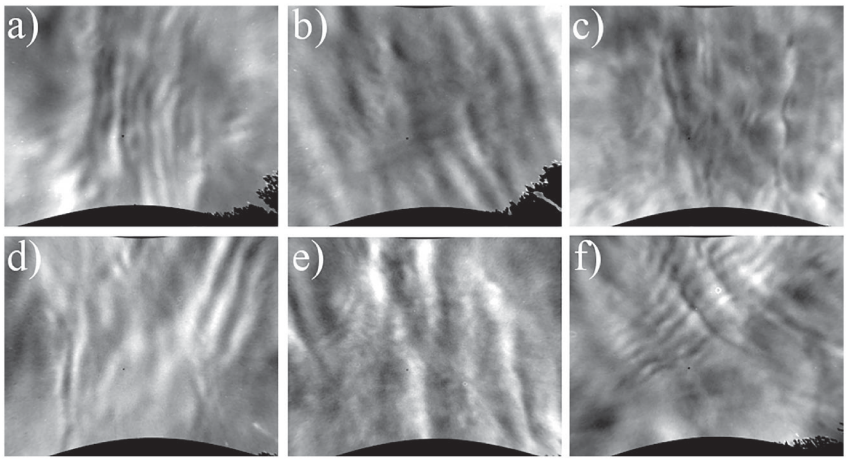

Figure 4. Series of Advanced Mesospheric Temperature Mapper brightness images illustrating the different types of structures and behaviors exhibited by MWs during the winter 2018. (a) localized short-scale waves, (b) extensive pattern covering the whole field-of-view, (c) "saw tooth" pattern, (d) coincident structure (a and c), (e) MW breaking, (f) streamwise vortices.

where c is the observed phase speed (~0 m/s in the case of MWs), U_h is the horizontal wind speed in the direction of the wave, $H = \mathrm{R.T_0/g}$ is the scale height (with $R = 287$ $\mathrm{Jkg^{-1}K^{-1}}$), and $k = 2\pi/\lambda_\mathrm{h}$ is the wave horizontal wavenumber. Finally, the vertical wavelength is given by $\lambda_z = 2\pi/\mathrm{m}$.

The uncertainty on the vertical wavenumber m is given by the equation

$$\Delta m = \sqrt{\left(\frac{N}{mU_h^2}\right)^2 \left(\Delta N\right)^2 + \left(\frac{N^2}{mU_h^3}\right)^2 \left(\Delta U_h\right)^2 + \left(\frac{k}{m}\right)^2 \left(\Delta k\right)^2 + \left(\frac{1}{4mH^3}\right)^2 \left(\Delta H\right)^2} \tag{4}$$

With the uncertainty on the scale height H equals to

$$\Delta H = \frac{H}{T_0}\Delta T_0 \tag{5}$$

Leading to an uncertainty on the vertical wavelength λ_z

$$\Delta\lambda_z = \frac{\lambda_z}{\mathrm{m}}\Delta\mathrm{m}. \tag{6}$$

Derived from Equation 1, the uncertainty on the MF $<u_h'w'>$ is given by

$$\Delta MF = \sqrt{\left(MF\frac{1-2\frac{\omega_i^2}{N^2}}{\omega_i\left(1-\frac{\omega_i^2}{N^2}\right)}\right)^2 \left(\Delta\omega_i\right)^2 + \left(MF\frac{4\frac{\omega_i^2}{N^2}-3}{N\left(1-\frac{\omega_i^2}{N^2}\right)}\right)^2 \left(\Delta N\right)^2 + \left(2\frac{MF}{\frac{\langle T'\rangle}{T_0}}\right)^2 \left(\Delta\frac{\langle T'\rangle}{T_0}\right)^2 + \left(2\frac{MF}{C}\right)^2 \left(\Delta C\right)^2} \tag{7}$$

With the uncertainties on the cancellation factor C, the relative temperature perturbation $<T'>/T_0$, and the intrinsic frequency ω respectively equal to

$$\Delta C = 7.12\left(\frac{z_{FWHM}}{\lambda_z}\right)C\Delta\lambda_z. \tag{8}$$

$$\Delta\frac{\langle T'\rangle}{T_0} = \frac{1}{T_0}\sqrt{\left(\Delta T'\right)^2 + \left(\Delta T_0\right)^2 . \left(\frac{T'}{T_0}\right)^2} \tag{9}$$

$$\Delta\omega = \sqrt{\left(\frac{\omega}{\lambda_h}\right)^2 \left(\Delta\lambda_h\right)^2 + \left(\frac{\omega}{U_h}\right)^2 \left(\Delta U_h\right)^2} \tag{10}$$

The uncertainties on the measurements are $\Delta<T'> = 1\mathrm{K}$, $\Delta T_0 = 3$ K, $\Delta\lambda_h = 3$ km, and $\Delta U_h = 3$ m/s. These values are typical for the AMTM and SAAMER instruments.

Figure 6 shows the distribution of the MW momentum fluxes over Rio Grande, during the Austral winter 2018. MF values were only obtained for 36 of the 97 identified MW events because the vertical wavelengths in the 61 other cases were indeterminate or very small (<<10 km) when calculated with Equation 3. In fact, Equation 3 only applies when the wave propagation follows the linear theory. If it gives a result corresponding to $\lambda_z < 10$ km, this result should be discarded because such wave should not be observable by an imager due to the integration over the thickness of the airglow layer. Usually, these cases correspond to waves encountering a critical level or overturning, as revealed by the "saw tooth" or breaking patterns often simultaneously observed in the image data. Table 1 presents the parameters, MF, and uncertainties for the 36 MW events for which Equations 1 and 3 could be reasonably applied.

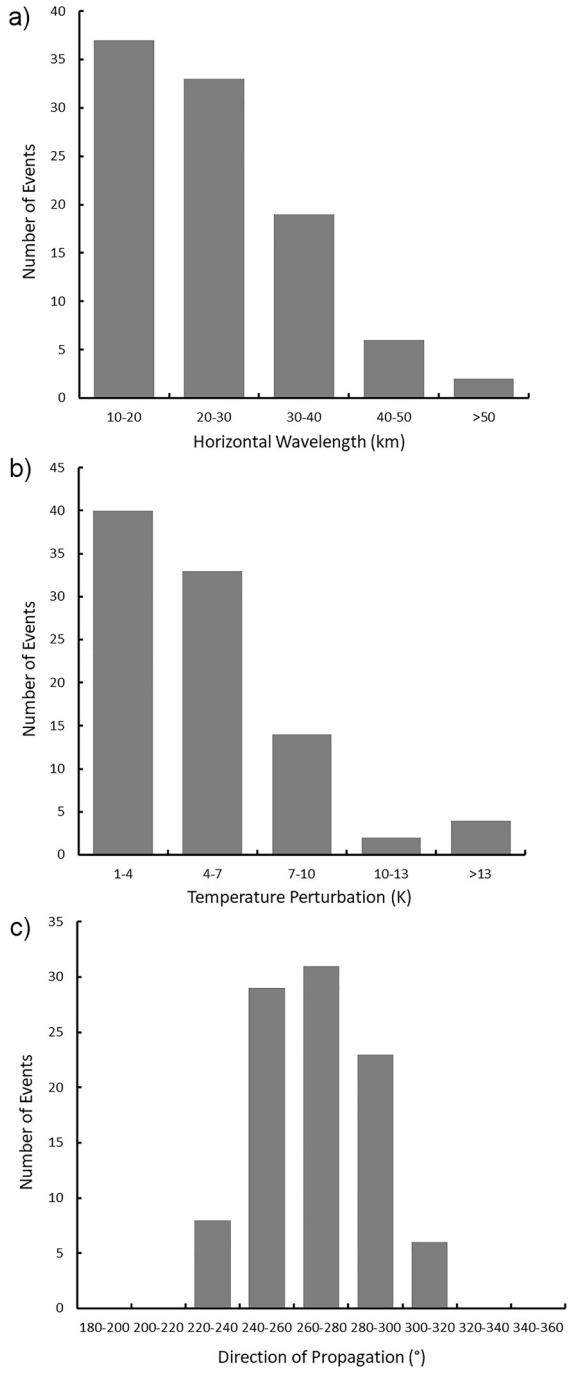

Figure 5. Mountain wave parameters distributions. (a) Horizontal wavelength, (b) temperature perturbation amplitude, and (c) direction of propagation.

The MF values in Figure 6 are consistently large compared to nonorographic GW MF studies (e.g., Cao & Liu, 2016; Suzuki et al., 2007; Tang et al., 2002; Vargas et al., 2009), ranging from ~14 to ~1,000 m^2/s^2, with an average value of 257 m^2/s^2, but only for 36 events. About half (44%) of the events had a MF < 100 m^2/s^2, but some more sporadic MWs reached values comparable to the largest MFs previously measured (Fritts et al., 2002; 2014; Taylor et al., 2019).

4. Discussion

4.1. Tropospheric Forcing

Mesospheric MWs over Rio Grande are generated in the troposphere when the eastward wind blows over the Southern Andes from the W and SW regions of Tierra del Fuego. Figure 7 shows the zonal wind between 0 and 15 km for March–September 2018, taken from operational analyses and short-term deterministic forecasts of Integrated Forecasting System of the European Center for Medium-Range Weather Forecasts (ECMWF). The model data are retrieved every 6 h at reduced spectral resolution of wavenumber 21 (~1,000 km horizontal resolution), and interpolated to the location of Rio Grande and to 500 m vertical intervals.

During the period shown in Figure 7, the zonal wind at 2 km (horizontal dashed line) was eastward ~95% of the time, providing almost continuous MW generation the whole winter. When only periods of mesospheric MW observations are taken into account, results are identical (~95%). However, not all the MW sightings correspond exactly to the presence of tropospheric forcing. This suggests that other factors, such as transient forcing or propagation conditions, or MW breaking at lower altitudes may prevent their attainment or clear identification in the MLT. The effects of the background atmosphere on the MW propagation, in particular wind filtering, must play a primary role in the observed MW intermittency.

4.2. Propagation Throughout the Middle Atmosphere

As they propagate upward from the troposphere, MWs are strongly affected by the state of the middle atmosphere, most importantly by the horizontal wind that could block their propagation to higher altitude. Figure 8a shows the ECMWF 6-h reanalysis horizontal wind amplitude from 0 to 70 km altitude, for June 2018, averaged over a 10° × 10° box centered on (80°W, 52.5°S). This location is the closest ECMWF data point to the Andes Mountains west of the observation site. Figure 8b presents the horizontal wind direction for the same location and period. Similar plots have been created for the other 5 months included in this study (not shown).

To let the MWs propagate upward, the horizontal wind has to stay eastward (Smith, 2019; Smith et al., 2009). To confirm that, Figure 9 plots the horizontal wind minima between 5 and 70 km in the opposite direction as the propagation of the 97 MWs, and at their time of observation. 85 events (87%) never encountered westward wind between 0 and 70 km (no significant differences using ECMWF data six hours earlier). The other 12 events have faced a westward wind component at some point (most of those waves occurred in mid-July). Nevertheless, wave propagation is not always linear and some events can go past critical levels due to nonlinear propagation effects (Fritts et al., 2019), interaction with other waves (Heale & Snively, 2015), or wave "leakage" (Heale et al., 2014). Of course, other elements can affect the MW propagation in the middle atmosphere, but these figures illustrate the fact that the middle

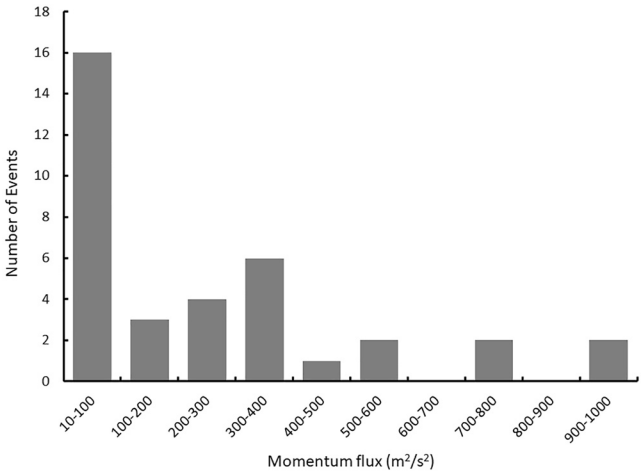

Figure 6. Momentum fluxes distribution for 36 mountain wave events.

atmospheric wind was highly favorable, as expected for this location and season, to MW propagation as high as the mesosphere.

4.3. Effects of the Semi-diurnal Tide

As seen for example in Figure 2, MWs were never visible over an entire night, even though the sky was perfectly clear and the tropospheric wind was blowing almost constantly over the mountains. To better understand the penetration of MWs to high altitudes, it is necessary to investigate the horizontal wind variability in the middle and upper atmosphere. Figure 10 shows the zonal wind measured by SAAMER between 80 and 100 km on the night of May 21 and 22, 2018 (same as Figure 2). The gray shading corresponds to daytime (no AMTM observations), and the blue shading to MWs visible in the airglow image data, which occur in association with periods of eastward wind in the lower part of the figure (~81–84 km). Furthermore, the wind direction appears to alternates from eastward to westward, with a ~12-h period, indicative of a semi-diurnal tide.

Semi-diurnal tide (SDT) mainly originates from the diurnal heating by solar radiation of the water vapor in the troposphere, and from the ozone in the upper stratosphere and lower mesosphere (Forbes, 1995). Like GWs, it too transports energy and momentum into the MLT, but it also modifies the atmospheric background, affecting the upward propagation of smaller-scale waves. While diurnal tide dominates at low latitudes because of latent heat release in convective processes, the SDT reaches its largest amplitude at mid-latitudes, around 50°, during winter (Hagan & Forbes, 2003; Hagan et al., 1999). Because of this, Rio Grande is an ideal location to study SDT activity. Indeed, using SAAMER data, Fritts, Janches, Iimura et al. (2010) have shown that SDT is larger than diurnal tide over Southern Argentina, reaching a first maximum in mean monthly amplitude between April and June (with values approaching 80–90 $m.s^{-1}$ above 95 km), and a second maximum between August and October.

Figure 11 summarizes the AMTM and SAAMER observations during the Austral winter 2018. The black line shows MW occurrence in the AMTM data for the period March 15–September 15, as a percentage of total clear sky time, for each 1-h bin between 21 UT and 12 UT. The red line is the average SAAMER zonal wind for the same period, between 81 and 84 km altitude. This altitude range corresponds to the bottom part of the OH layer, that is, the lowest altitude where MWs can be detected by the AMTM. Figure 11 shows high correlation between the airglow MW occurrence and the mesospheric zonal wind variability driven by the SDT, with an almost 12-h period.

Critical level filtering due to winds approaching $U_h = 0$ m/s plays an important role in GW propagation. If $U_h >> 0$ m/s, λ_z is large (see Equation 3), and the GW will freely propagate, transporting momentum to a higher/lower altitude (in the case of an upward/downward-propagating wave). If U_h is approaching 0 m/s (critical level), λ_z will be very small and likely exhibit instabilities that further constrain the amplitude and the airglow response. In the case of MWs, the eastward wind allows MW propagation to higher levels, while westward wind blocks the waves at a lower altitude, acting like a gate to the upper atmosphere.

However, eastward wind at 80 km and above does not always yield MW observations. In fact, MWs were recorded in the AMTM data only 29.5% of the time the zonal wind was positive (considering only clear sky conditions), which means that other parameters are important for the MW penetration up to the mesosphere. Recent studies have revealed the effects of several of those parameters. The first one is the horizontal wind minima around 15–25 km, dubbed a "valve layer," which can attenuate the MWs amplitude and filters part of the wave spectrum, thus allowing MW to propagate to higher altitudes, but with amplitudes attenuated at lower altitudes (Kaifler et al., 2015; Kruse et al., 2016). Another factor can also have a large effect on MW propagation around 45–55° latitude: The Polar Night Jet, with strong eastward winds between 40 and 70 km, can partially reflect MWs having sufficiently small λ_hs, or even trap them at the stratopause altitude where $m^2 < 0$ for sufficiently large U_h and/or k (see Equation 3) (Bramberger et al., 2017). Finally, Taylor et al. (2019) have shown that a 4-hr GW in the MLT modulating larger-scale wind allowed a spectacular large-amplitude MW to reach the OH layer altitude over the New Zealand South Island on June 21, 2014.

Table 1
Parameters for the 36 MW Events for Which the MF was Calculated

Date	Duration (hr)	Uh (m/s)	λh (km)	T0 (K)	<T'> (K)	Peak MF (m^2/s^2)	ΔMF (m^2/s^2)
April 05–06	04:00	−32.2	17.9	204.4	2.8	96	76
April 27–28	03:00	−28.0	29.6	189.9	2.1	245	252
April 30–01	09:00	−29.0	30.6	184.9	1.6	99	138
May 06–07	08:00	−25.1	16.1	199.2	2.0	323	361
May 20–21	10:00	−34.8	16.2	202.5	6.1	241	101
May 27–28	01:00	−30.8	16.7	203.0	2.3	76	72
June 01–02	04:00	−49.3	22.5	212.9	5.8	88	36
June 02–03	02:00	−32.4	35.7	209.1	1.9	55	62
June 11–12	02:00	−40.4	19.1	202.1	8.5	307	109
June 11–12	06:00	−32.5	33.6	204.1	4.9	375	221
June 12–13	01:30	−24.9	25.5	213.1	2.8	957	892
June 13–14	01:50	−31.4	15.8	191.3	7.5	716	298
June 16–17	11:00	−58.2	23.7	199.9	7.9	129	39
June 18–19	05:00	−33.5	12.4	193.3	3.8	45	30
Jun 19–20	03:00	−40.2	35.2	192.0	7.0	315	147
Jun 26–27	05:00	−33.9	11.2	193.3	4.1	19	48
Jun 28–29	02:30	−34.4	15.3	206.2	4.9	139	65
Jun 29–30	01:00	−52.0	18.3	184.4	3.4	19	15
July 01–02	07:00	−33.4	18.8	206.7	9.8	995	404
July 03–04	01:00	−25.5	12.2	204.7	2.9	231	182
July 03–04	02:00	−42.6	24.0	194.6	4.2	89	49
July 07–08	03:00	−41.6	20.8	189.1	8.2	335	122
July 13–14	03:00	−37.3	35.0	191.0	8.0	553	252
July 13–14	03:00	−34.5	23.6	188.9	8.0	789	365
July 16–17	08:00	−52.7	19.1	200.4	5.5	47	24
July 17–18	05:30	−35.7	28.5	203.0	4.3	180	108
July 18–19	02:15	−55.8	21.5	201.6	2.9	15	11
July 31–August 01	03:30	−38.9	38.4	206.8	3.8	90	57
July 31–August 01	03:30	−38.9	13.9	208.5	3.9	28	20
July 31–August 01	01:30	−42.2	13.9	210.4	7.0	39	91
August 04–05	05:00	−24.4	10.8	197.5	4.6	577	309
August 26–27	03:00	−44.5	28.8	193.7	7.5	271	110
August 29–30	01:45	−33.9	46.6	196.0	5.2	329	175
August 30–31	01:00	−44.8	15.8	189.8	4.6	37	27
September 01–02	01:00	−25.9	28.6	214.2	2.2	404	431
September 05–06	01:10	−35.4	23.6	193.0	1.3	18	29
		ΔUh = 3 m/s	Δλh = 3 km	ΔT0 = 3 K	Δ<T'> = 1 K		

Our observations and discussion reveal that many factors contribute to the complexity of MW propagation into the MLT over a mountainous region in winter conditions. Of the various influences, however, the SDT appears to be the main driver accounting for MW nightly intermittency over Southern Argentina.

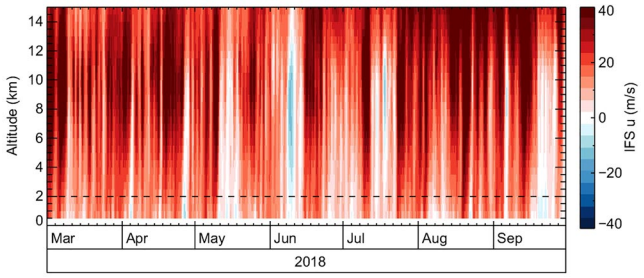

Figure 7. European Center for Medium-Range Weather Forecasts tropospheric zonal wind between March and September 2018.

4.4. Mountain Waves Momentum Flux

The important role played by GWs in the upper atmosphere can be estimated by assessing their transport of energy and momentum. GW dissipation yields pseudo-momentum deposition that contributes, for example, to the reversal of the mesospheric jets, the residual circulation from the troposphere to the mesosphere, and systematic influences on the large-scale circulation and thermal structures at these altitudes (Fritts & Alexander, 2003).

The MW MFs measured at Rio Grande and presented in Figure 6 correspond to the maximum for each event. In general, these events evolved over the time they were observed in the AMTM data, because of the variability in the forcing, the horizontal background wind, or the effects of wave breaking which reduces the wave amplitude, therefore

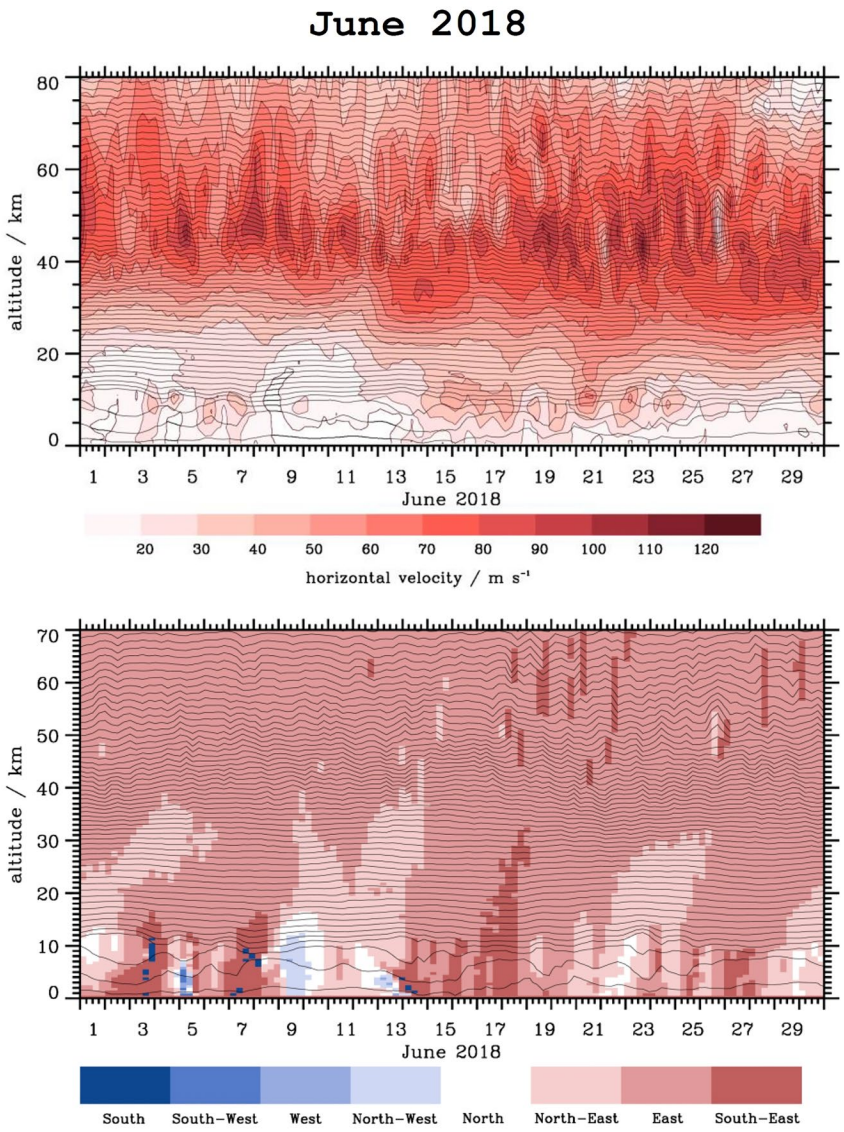

Figure 8. (a) Six-hour European Center for Medium-Range Weather Forecasts re-analysis horizontal wind amplitude between 0 and 70 km, for June 2018, averaged over a 10° × 10 ° box centered on (80°W, 52.5°S), (b) corresponding horizontal wind direction.

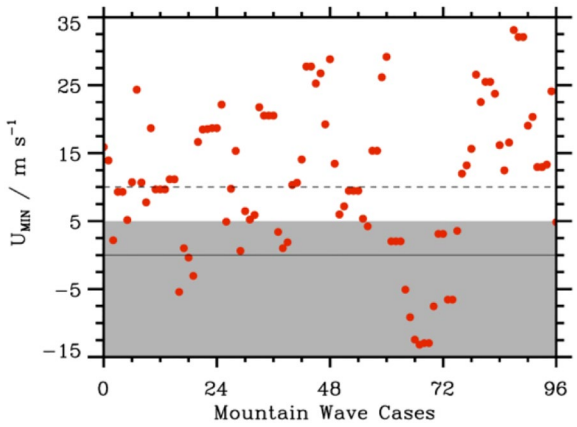

Figure 9. Horizontal wind minima between 5 and 70 km, in the opposite direction of propagation for each of 97 mountain waves, and at their time of observation.

decreasing the MF (Fritts et al., 2009; Taylor et al., 2019). In addition, MF estimates are subject to significant measurement uncertainties up to ~35% or greater (Vargas, 2018). However, the goal of this study is not to provide a detailed, case-by-case analysis of each MW event and its associated MF, but to reveal their intermittency and their anticipated large impacts in the MLT over the Southern Andes. Indeed, Figure 6 shows that the 36 MW events included in this plot had extremely large MFs. The average value (~250 m^2/s^2), although for a limited number of cases, was much larger than previous mesospheric GW studies (e.g., Suzuki et al., 2007; Tang et al., 2002; Vargas et al., 2009). Furthermore, a few rare events had MF >500 m^2/s^2. The importance of these waves has been previously revealed in the stratosphere by balloon measurements obtained over Antarctica. Hertzog et al. (2012) recorded sporadic, very strong events over mountainous regions, such as the Antarctic Peninsula or the Trans-Antarctic Mountain chain. Most importantly, the 1% largest events accounted for ~25% of the total MF during the winter season. Wright et al. (2013) confirmed this result on a near-global scale using satellite data.

The current study shows that, in the MLT as well, such extremely large waves exist over a mountainous region like the Southern Andes where they are generated by orographic forcing. Their MF is much larger than for nonorographic GWs, implying a tremendous impact on the upper atmosphere.

Wright et al. (2013) have also shown that GW intermittency seems to decrease with increasing altitude between 25 and 65 km, attributing this result to the interactions between the waves and the background atmosphere as they propagate away from their sources. Using mesospheric airglow imaging, Cao and Liu (2016) investigated GW MFs and intermittency over two very different locations: Maui, Hawaii (20.8°N, in the Pacific Ocean), and Cerro Pachón, Chile (30.2°S, in the Andes Mountains). Unexpectedly, they found that intermittency was larger over the ocean site, in contrast with stratospheric observations. They explain this result by the possible differences in the propagation conditions between the two sites.

The MW observations over Tierra del Fuego reveal that the GW intermittency is significant over this hotspot, with large, occasional events carrying considerable MF. The intermittency does not depend only on the MW generation, as the tropospheric forcing is almost permanent, but is also highly correlated with the background atmosphere variability, especially the wind filtering in the MLT due to the SDT.

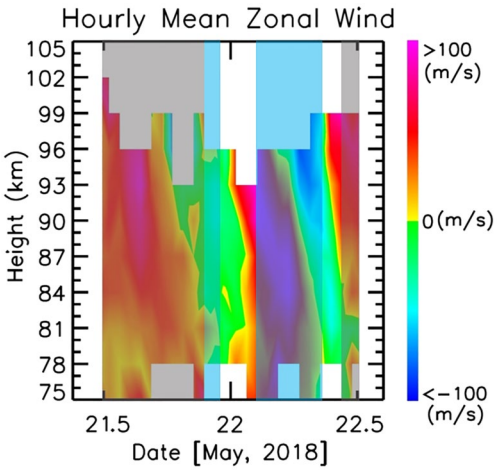

Figure 10. Southern Argentina Agile MEteor Radar zonal wind data for May 21 and 22, 2018. The gray shading corresponds to daytime (no AMTM data), and the blue shading to mountain waves observations.

5. Conclusion

Previous satellite measurements have shown that MWs regularly reach the middle and upper stratosphere over the South America-Drake Passage-Antarctic Peninsula hotspot region (e.g., Jiang et al., 2002, 2003, 2005). This study presents recent multi-instrument observations conducted in the lee of the Southern Andes during the Austral winter 2018. To our knowledge, this is the first extensive investigation of mesospheric MWs covering a complete winter season. The main results are as follows:

- Penetration of MWs as high as the MLT is relatively common. More than 90 events were detected with the USU AMTM imager during a 6-month period, corresponding to ~25% of the clear sky time, with a peak frequency>35% from mid-May to mid-July
- MW occurrence is highly correlated with the eastward phase of the semi-diurnal tide, which strongly modulates the total eastward wind in the MLT, acting as a gate and modulating the penetration of MF into the upper atmosphere

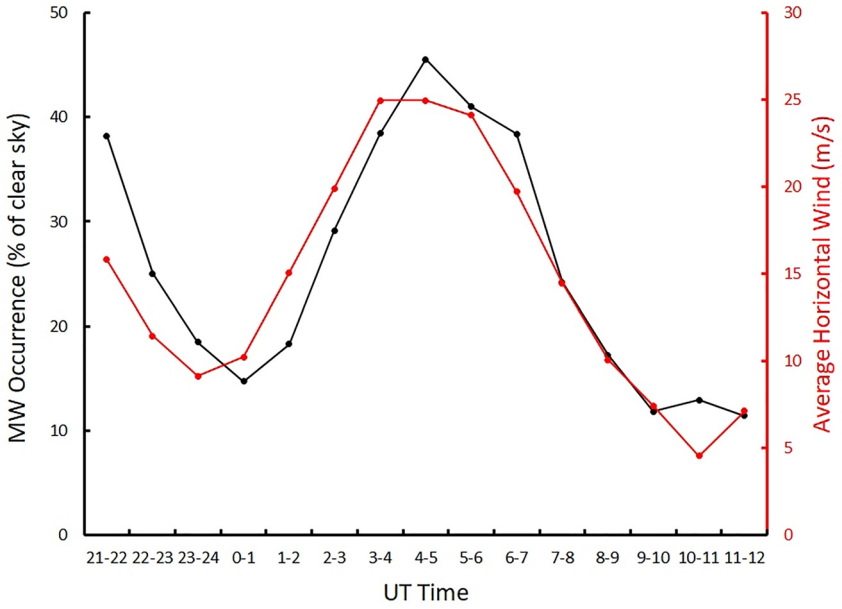

Figure 11. Correlation between nightly average mountain waves occurrence and average zonal wind at 81–84 km, for the Austral winter 2018.

- Nevertheless, as the tropospheric forcing is almost permanent in this region, but MWs are not always visible even when the MLT zonal wind is eastward, other processes must also influence MW penetration into the MLT, such as the Polar Night Jet
- MW MFs are large, with an average of ~250 m^2/s^2 for 36 of the 97 events. Even though the number of cases is limited, the result still provides new evidence of the importance and frequent impacts of MWs on the MLT over this region

The near permanent orographic forcing in this part of the world makes Southern Argentina an ideal location to study MW life cycles and the various environmental and dynamical influences. The cluster of aeronomy instruments operating in Tierra del Fuego offers an exceptional opportunity to investigate the complexity of MW deep propagation at this prominent high-latitude site, with extended nighttime airglow observations during the winter season.

Future case-by-case studies involving measurements and model simulations are now needed to help understand the effects of each of the components associated with the complex MW propagation mechanism.

Acknowledgments
The AMTM operated at Rio Grande was designed and built at Utah State University (USU) and the Space Dynamics Laboratory (SDL) with support from the NSF DEEPWAVE Grant 1061892. It is currently operated under NSF Grant 1651233. D. Janches's work is supported by the NASA ISFM Heliophysics Program. SAAMER's operation is supported by the NASA SSO Program, NESC assessment TI-17-01204, and NSF grant AGS-1647354. SAAMER data are available on http://cedar.openmadrigal.org.The authors would like to thank the personnel at the Rio Grande Astronomical Observatory (EARG) for their help in installing and operating the AMTM, SAAMER, and CORAL instruments, in particular the invaluable support of Carlos Ferrer, Gerardo Connon, and Luis Barbero.

Data Availability Statement

The AMTM data used in this study are available through the Harvard Dataverse repository (https://doi.org/10.7910/DVN/FADJPL). The ECMWF data are freely accessible (Creative Commons 4.0 license CC-BY-4.0) on the following website: https://apps.ecmwf.int/archive-catalogue/

References

Alexander, M. J., & Teitelbaum, H. (2011). Three-dimensional properties of Andes mountain waves observed by satellite: A case study. *Journal of Geophysical Research*, *116*, D23110. https://doi.org/10.1029/2011JD016151

Bossert, K., Fritts, D. C., Pautet, P. D., Williams, B. P., Taylor, M. J., Kaifler, B., et al. (2015). Momentum flux estimates accompanying multiscale gravity waves over Mount Cook, New Zealand, on 13 July 2014 during the DEEPWAVE campaign. *Journal of Geophysical Research - D: Atmospheres*, *120*, 9323–9337. https://doi.org/10.1002/2015JD023197

Bossert, K., Kruse, C. G., Heale, C. J., Fritts, D. C., Williams, B. P., Snively, J. B., et al. (2017). Secondary gravity wave generation over New Zealand during the DEEPWAVE campaign. *Journal of Geophysical Research - D: Atmospheres*, *122*, 7834–7850. https://doi.org/10.1002/2016JD026079

Bramberger, M., Dörnbrack, A., Bossert, K., Ehard, B., Fritts, D. C., Kaifler, B., et al. (2017). Does strong tropospheric forcing cause large-amplitude mesospheric gravity waves? A DEEPWAVE case study. *Journal of Geophysical Research - D: Atmospheres*, *122*(21), 11422–11443. https://doi.org/10.1002/2017JD027371

Cao, B., & Liu, A. Z. (2016). Intermittency of gravity wave momentum flux in the mesopause region observed with an all-sky airglow imager. *Journal of Geophysical Research - D: Atmospheres*, *121*(2), 650–663. https://doi.org/10.1002/2015JD023802

de Wit, R. J., Janches, D., Fritts, D. C., & Hibbins, R. E. (2016). QBO modulation of the mesopause gravity wave momentum flux over Tierra del Fuego. *Geophysical Research Letters*, *43*(8), 4049–4055. https://doi.org/10.1002/2016GL068599

de Wit, R. J., Janches, D., Fritts, D. C., Stockwell, R. G., & Coy, L. (2017). Unexpected climatological behavior of MLT gravity wave momentum flux in the lee of the Southern Andes hot spot. *Geophysical Research Letters*, *44*(2), 1182–1191. https://doi.org/10.1002/2016GL072311

Dörnbrack, A., Birner, T., Fix, A., Flentje, H., Meister, A., Schmid, H., et al. (2002). Evidence for inertia gravity waves forming polar stratospheric clouds over Scandinavia. *Journal of Geophysical Research*, *107*(D20), SOL 30-1–SOL 30-18. https://doi.org/10.1029/2001JD000452

Dörnbrack, A., Leutbecher, M., Kivi, R., & Kyrö, E. (1999). Mountain-wave-induced record low stratospheric temperatures above northern Scandinavia. *Tellus A*, *51*(5), 951–963. https://doi.org/10.3402/tellusa.v51i5.14504

Eckermann, S. D., Broutman, D., Ma, J., Doyle, J. D., Pautet, P.-D., Taylor, M. J., et al. (2016). Dynamics of orographic gravity waves observed in the mesosphere over the Auckland Islands during the Deep Propagating Gravity Wave Experiment (DEEPWAVE). *Journal of the Atmospheric Sciences*, *73*(10), 3855–3876. https://doi.org/10.1175/JAS-D-16-0059.1

Eckermann, S. D., & Preusse, P. (1999). Global measurements of stratospheric mountain waves from space. *Science*, *286*(5444), 1534–1537. https://doi.org/10.1126/science.286.5444.1534

Ejiri, M. K., Shiokawa, K., Ogawa, T., Igarashi, K., Nakamura, T., & Tsuda, T. (2003). Statistical study of short-period gravity waves in OH and OI nightglow images at two separated sites. *Journal of Geophysical Research*, *108*(D21), 4679. https://doi.org/10.1029/2002JD002795

Eliassen, A., & Palm, E. (1960). On the transfer of energy in stationary mountain waves. *Geofysiske Publikasjoner*, *22*, 1–23

Forbes, J. M. (1995). Tidal and planetary waves. In R. M. Johnson, & T. L. Killeen, (Eds.), The upper mesosphere and lower thermosphere: A review of experiment and theory, Geophysics monography series 87 (pp. 67–87). AGU.

Fritts, D. C., & Alexander, M. J. (2003). Gravity wave dynamics and effects in the middle atmosphere. *Reviews of Geophysics*, *41*(1), 1003. https://doi.org/10.1029/2001RG000106

Fritts, D. C., Janches, D., & Hocking, W. K. (2010a). Southern Argentina agile meteor radar: Initial assessment of gravity wave momentum fluxes. *Journal of Geophysical Research*, *115*, D19123. https://doi.org/10.1029/2010JD013891

Fritts, D. C., Janches, D., Iimura, H., Hocking, W. K., Mitchell, N. J., Stockwell, R. G., et al. (2010b). Southern Argentina agile meteor radar: System design and initial measurements of large-scale winds and tides. *Journal of Geophysical Research*, *115*(D18). https://doi.org/10.1029/2010JD013850

Fritts, D. C., & Nastrom, G. D. (1992). Sources of mesoscale variability of gravity waves. Part II: Frontal, convective, and jet stream excitation. *Journal of the Atmospheric Sciences*, *49*(2), 111–127. https://doi.org/10.1175/1520-0469(1992)049<0111:somvog>2.0.co;2

Fritts, D. C., Pautet, P.-D., Bossert, K., Taylor, M. J., Williams, B. P., Iimura, H., et al. (2014). Quantifying gravity wave momentum fluxes with mesosphere temperature mappers and correlative instrumentation. *Journal of Geophysical Research - D: Atmospheres*, *119*(14), 13583–13603. https://doi.org/10.1002/2014JD022150

Fritts, D. C., Smith, R. B., Taylor, M. J., Doyle, J. D., Eckermann, S. D., Dörnbrack, A., et al. (2016). The Deep Propagating Gravity Wave Experiment (DEEPWAVE): An airborne and ground-based exploration of gravity wave propagation and effects from their sources throughout the lower and middle atmosphere. *Bulletin of the American Meteorological Society*, *97*(3), 425–453. https://doi.org/10.1175/BAMS-D-14-00269.1

Fritts, D. C., Vadas, S. L., & Yamada, Y. (2002). An estimate of strong local body forcing and gravity wave radiation based on OH airglow and meteor radar observations. *Geophysical Research Letters*, *29*(10), 71-1–71-4. https://doi.org/10.1029/2001GL013753

Fritts, D. C., Vosper, S. B., Williams, B. P., Bossert, K., Plane, J. M. C., Taylor, M. J., et al. (2018). Large-amplitude mountain waves in the mesosphere accompanying weak cross-mountain flow during DEEPWAVE Research Flight RF22, *Journal of Geophysical Research - D: Atmospheres*, *123*(18), 9992–10022. https://doi.org/10.1029/2017JD028250

Fritts, D. C., Wang, L., Taylor, M. J., Pautet, P. -D., Criddle, N. R., Kaifler, B., et al. (2019). Large-amplitude mountain waves in the mesosphere observed on 21 June 2014 during DEEPWAVE: 2. Nonlinear dynamics, wave breaking, and instabilities. *Journal of Geophysical Research: Atmosphere*, *124*(17–18), 10006–10032. https://doi.org/10.1029/2019jd030899

Fritts, D. C., Wang, L., Werne, J., Lund, T., & Wan, K. (2009). Gravity wave instability dynamics at high Reynolds numbers. Part I: Wave field evolution at large amplitudes and high frequencies, *Journal of the Atmospheric Sciences*, *66*(5), 1126–1148, https://doi.org/10.1175/2008JAS2726.1

Grubišić, V., Doyle, J. D., Kuettner, J., Mobbs, S., Smith, R. B., Whiteman, C. D., et al. (2008). The Terrain-Induced Rotor Experiment: A field campaign overview including observational highlights, *Bulletin of the American Meteorological Society*, *89*(10), 1513–1533. https://doi.org/10.1175/2008BAMS2487.1

Hagan, M. E., Burrage, M. D., Forbes, J. M., Hackney, J., Randel, W. J., & Zhang, X. (1999). GSWM-98: Results for migrating solar tides. *Journal of Geophysical Research*, *104*(A4), 6813–6827. https://doi.org/10.1029/1998ja900125

Hagan, M. E., & Forbes, J. M. (2003). Migrating and nonmigrating semidiurnal tides in the upper atmosphere excited by tropospheric latent heat release. *Journal of Geophysical Research*, *108*(A2), 1062. https://doi.org/10.1029/2002JA009466

Heale, C. J., & Snively, J. B. (2015). Gravity wave propagation through a vertically and horizontally inhomogeneous background wind. *Journal of Geophysical Research - D: Atmospheres*, *120*(12), 5931–5950. https://doi.org/10.1002/2015JD023505

Heale, C. J., Snively, J. B., & Hickey, M. P. (2014). Numerical simulation of the long-range propagation of gravity wave packets at high latitudes. *Journal of Geophysical Research - D: Atmospheres*, *119*(19), 116. https://doi.org/10.1002/2014JD022099

Hecht, J. H., Fritts, D. C., Wang, L., Gelinas, L. J., Rudy, R. J., Walterscheid, R. L., et al. 2018). Observations of the breakdown of mountain waves over the Andes Lidar Observatory at Cerro Pachon on 8/9 July 2012. *Journal of Geophysical Research - D: Atmospheres*, *123*(1), 276–299. https://doi.org/10.1002/2017JD027303

Hecht, J. H., Walterscheid, R. L., Hickey, M. P., & Franke, S. J. (2001). Climatology and modeling of quasi-monochromatic atmospheric gravity waves observed over Urbana Illinois. *Journal of Geophysical Research*, *106*(D6), 5181–5195. https://doi.org/10.1029/2000jd900722

Hendricks, E. A., Doyle, J. D., Eckermann, S. D., Jiang, Q., & Reinecke, P. A. (2014). What is the source of the stratospheric gravity wave belt in Austral winter?. *Journal of the Atmospheric Sciences*, *71*(5), 1583–1592. https://doi.org/10.1175/JAS-D-13-0332.1

Hertzog, A., Alexander, M. J., & Plougonven, R. (2012). On the intermittency of gravity wave momentum flux in the stratosphere. *Journal of the Atmospheric Sciences*, *69*(11), 3433–3448. https://doi.org/10.1175/jas-d-12-09.1

Jiang, J. H., Eckermann, S. D., Wu, D. L., Hocke, K., Wang, B., Ma, J., & Zhang, Y. (2005). Seasonal variation of gravity wave sources from satellite observation. *Advances in Space Research*, *35*(11), 1925–1932. https://doi.org/10.1016/j.asr.2005.01.099

Jiang, J. H., Wu, D. L., & Eckermann, S. D. (2002). Upper Atmosphere Research Satellite (UARS) MLS observation of mountain waves over the Andes. *Journal of Geophysical Research*, *107*(D20), SOL 15-1–SOL 15-10. https://doi.org/10.1029/2002JD002091

Jiang, J. H., Wu, D. L., Eckermann, S. D., & Ma, J. (2003). Mountain waves in the middle atmosphere: microwave limb sounder observations and analyses. *Advances in Space Research*, *32*(5), 801–806. https://doi.org/10.1016/s0273-1177(03)00402-2

Kaifler, B., Kaifler, N., Ehard, B., Dörnbrack, A., Rapp, M., & Fritts, D. C. (2015). Influences of source conditions on mountain wave penetration into the stratosphere and mesosphere. *Geophysical Research Letters*, *42*(21), 8791–9590. https://doi.org/10.1002/2015GL066465

Kruse, C. G., Smith, R. B., & Eckermann, S. D. (2016). The midlatitude lower-stratospheric mountain wave "Valve Layer", *Journal of the Atmospheric Sciences*, *73*(12), 5081–5100. https://doi.org/10.1175/JAS-D-16-0173.1

Küttner, J. (1939a). Moazagotl und föhnwelle. *Beiträge zur Physik der freien Atmosphäre*, *25*, 79–114

Küttner, J. (1939b). Zur entstehung der föhnwelle. *Beiträge zur Physik der freien Atmosphäre*, *25*, 251–299

Nappo, C. J. (2002). *Atmospheric Gravity Waves, International Geophysical Series*. Academic Press.

Pautet, P.-D., Taylor, M. J., Fritts, D. C., Bossert, K., Williams, B. P., Broutman, D., et al. (2016). Large-amplitude mesospheric response to an orographic wave generated over the Southern Ocean Auckland Islands (50.7°S) during the DEEPWAVE project. *Journal of Geophysical Research - D: Atmospheres*, *121*(4), 1431–1441. https://doi.org/10.1002/2015JD024336

Pautet, P.-D., Taylor, M. J., Pendleton, W. R., Zhao, Y., Yuan, T., Esplin, R., & McLain, D. (2014). Advanced mesospheric temperature mapper for high-latitude airglow studies. *Applied Optics*, *53*(26), 5934–5943. https://doi.org/10.1364/ao.53.005934

Pautet, P.-D., Taylor, M. J., Snively, J. B., & Solorio, C. (2018). Unexpected occurrence of mesospheric frontal gravity wave events over south pole (90°S), *Journal of Geophysical Research - D: Atmospheres*, *123*(1), 160–173. https://doi.org/10.1002/2017JD027046

Plougonven, R., Hertzog, A., & Teitelbaum, H. (2008). Observations and simulations of a large-amplitude mountain wave breaking over the Antarctic Peninsula. *Journal of Geophysical Research*, *113*(D16). https://doi.org/10.1029/2007JD009739

Schoeberl, M. R. (1985). The penetration of mountain waves into the middle atmosphere. *Journal of the Atmospheric Sciences*, *42*(24), 2856–2864. https://doi.org/10.1175/1520-0469(1985)042<2856:tpomwi>2.0.co;2

Scorer, R. S. (1949). Theory of waves in the lee of mountains. *Quarterly Journal of the Royal Meteorological Society*, *75*(323), 41–56. https://doi.org/10.1002/qj.49707532308

Smith, R. B. (1980). Linear theory of stratified hydrostatic flow past an isolated mountain. *Tellus*, *32*, 348–364. https://doi.org/10.1111/j.2153-3490.1980.tb00962.x10.3402/tellusa.v32i4.10590

Smith, R. B. (2019). *100 years of progress on mountain meteorology research*. American Meteorological Society. https://doi.org/10.1175/AMSMONOGRAPHS-D-18-0022.1

Smith, S., Baumgardner, J., & Mendillo, M. (2009). Evidence of mesospheric gravity-waves generated by orographic forcing in the troposphere. *Geophysical Research Letters*, *36*, L08807. https://doi.org/10.1029/2008GL036936

Snively, J. B., Nielsen, K., Hickey, M. P., Heale, C. J., Taylor, M. J., & Moffat-Griffin, T. (2013). Numerical and statistical evidence for long-range ducted gravity wave propagation over Halley, Antarctica. *Geophysical Research Letters*, *40*(18), 4813–4817. https://doi.org/10.1002/grl.50926

Stockwell, R. G., & Lowe, R. P. (2001). Airglow imaging of gravity waves: 1. Results from a small network of OH nightglow scanning imagers. *Journal of Geophysical Research*, *106*(D15). 17185–17203. https://doi.org/10.1029/2001jd900035

Suzuki, S., Shiokawa, K., Otsuka, Y., Ogawa, T., Kubota, M., Tsutsumi, M., et al. (2007). Gravity wave momentum flux in the upper mesosphere derived from OH airglow imaging measurements. *Earth Planet Sp*, *59*, 421–428. https://doi.org/10.1186/bf03352703

Tang, J., Liu, A. Z., & Swenson, G. R. (2002). High frequency gravity waves observed in OH airglow at Starfire Optical Range, NM: Seasonal variations in momentum flux. *Geophysical Research Letters*, *29*(20), 27-1–27-4. https://doi.org/10.1029/2002GL015794

Taylor, M. J., Pautet, P.-D., Fritts, D. C., Kaifler, B., Smith, S. M., Zhao, Y., et al. (2019). Large-amplitude mountain waves in the mesosphere observed on 21 June 2014 during DEEPWAVE: 1. Wave development, scales, momentum fluxes, and environmental sensitivity, *Journal of Geophysical Research - D: Atmospheres*, *124*(19), 10364–10384. https://doi.org/10.1029/2019JD030932

Taylor, M. J., Pautet, P.-D., Medeiros, A. F., Buriti, R., Fechine, J., Fritts, D. C., et al. (2009). Characteristics of mesospheric gravity waves near the magnetic equator, Brazil, during the SpreadFEx campaign. *Annales Geophysicae*, *27*(2), 461–472. https://doi.org/10.5194/angeo-27-461-2009

Vadas, S. L., Xu, S., Yue, J., Bossert, K., Becker, E., & Baumgarten, G. (2019). Characteristics of the quiet-time hot spot gravity waves observed by GOCE over the Southern Andes on 5 July 2010. *Journal of Geophysical Research Space Physics*, *124*(8), 7034–7061. https://doi.org/10.1029/2019JA026693

Vargas, F. (2019). Uncertainties in gravity wave parameters, momentum fluxes, and flux divergences estimated from multi-layer measurements of mesospheric nightglow layers. *Advances in Space Research*, *63*(2), 967–985. https://doi.org/10.1016/j.asr.2018.09.039

Vargas, F., Gobbi, D., Takahashi, H., & Lima, L. M. (2009). Gravity wave amplitudes and momentum fluxes inferred from OH airglow intensities and meteor radar winds during SpreadFEx. *Annales Geophysicae*, *27*, 1–9. https://doi.org/10.5194/angeo-27-2361-2009

Wright, C. J., Hindley, N. P., Moss, A. C., & Mitchell, N. J. (2016). Multi-instrument gravity-wave measurements over Tierra del Fuego and the drake passage - Part 1: Potential energies and vertical wavelengths from AIRS, COSMIC, HIRDLS, MLS-Aura, SAAMER, SABER, and radiosondes. *Atmospheric Measurement Techniques*, *9*, 877–908. https://doi.org/10.5194/amt-9-877-2016

Wright, C. J., Osprey, S. M., & Gille, J. C. (2013). Global observations of gravity wave intermittency and its impact on the observed momentum flux morphology. *Journal of Geophysical Research - D: Atmospheres*, *118*(19). 10980–10993. https://doi.org/10.1002/jgrd.50869

Wu, D. L., Preusse, P., Eckermann, S. D., Jiang, J. H., Juarez, M. d. l. T., Coy, L., & Wang, D. Y. (2006). Remote sounding of atmospheric gravity waves with satellite limb and nadir techniques. *Advances in Space Research*, *37*(12), 2269–2277. https://doi.org/10.1016/j.asr.2005.07.031

Zhao, Y., Taylor, M. J., Pautet, P. D., Moffat-Griffin, T., Hervig, M. E., Murphy, D. J., et al. (2019). Investigating an unusually large 28-day oscillation in mesospheric temperature over Antarctica using ground-based and satellite measurements, *Journal of Geophysical Research - D: Atmospheres*, *124*(15), 8576–8593, https://doi.org/10.1029/2019JD030286